



Pairs, trimers, and BCS-BEC crossover near a flat band: Sawtooth latticeGiuliano Orso ^{1,*} and Manpreet Singh^{2,1}¹*Université de Paris, Laboratoire Matériaux et Phénomènes Quantiques, CNRS, F-75013 Paris, France*²*Centre for Quantum Engineering Research and Education, TCG Centres for Research and Education in Science and Technology, Sector V, Salt Lake, Kolkata 700091, India* (Received 21 December 2021; revised 25 March 2022; accepted 21 June 2022; published 6 July 2022)

We investigate pairing and superconductivity in the attractive Fermi-Hubbard model on the one-dimensional sawtooth lattice, which exhibits a flat band by fine-tuning the hopping rates. We first solve the two-body problem, both analytically and numerically, to extract the binding energy and the effective mass of the pairs. Based on the density matrix renormalization group method, we address the ground-state properties of the many-body system, assuming equal spin populations. We compare our results with those available for a linear chain, where the model is integrable by the Bethe ansatz, and we show that the multiband nature of the system substantially modifies the physics of the BCS-BEC crossover. We find that near a flat band, the chemical potential remains always close to its zero-density limit predicted by two-body physics. In contrast, the pairing gap exhibits a remarkably strong density dependence and, differently from the pair binding energy, it is no longer peaked at the flat-band point. We show that these results can be interpreted in terms of polarization screening effects, due to an anomalous attraction between pairs in the medium and single fermions. Importantly, we unveil that three-body bound states (trimers) exist in the sawtooth lattice, in sharp contrast with the linear chain geometry, and we compute their binding energy. The nature of these states is investigated via a strong-coupling variational approach, revealing that they originate from tunneling-induced exchange processes.

DOI: [10.1103/PhysRevB.106.014504](https://doi.org/10.1103/PhysRevB.106.014504)**I. INTRODUCTION**

During the past ten years, there has been a growing interest in flat-band (FB) lattices [1]. These are periodic systems, described by tight-binding models, in which one or more dispersion relation is flat or almost flat. The corresponding eigenstates are localized on a few lattice sites due to destructive quantum interference. The absence of kinetic energy together with the inherent macroscopic degeneracy make FB systems ideal candidates to enhance interaction effects. For instance they provide a viable route to enhance the superconducting transition temperature [2–5], generate fractional quantum Hall states at room temperature [6], and produce many other intriguing quantum effects.

Lattice models containing a flat band have been realized experimentally with optical lattices for ultracold atoms [7–9], photonic lattices [10,11], semiconductor microcavities [12], and artificial electronic lattices [13–15]. The recent discovery [16] of unconventional superconductivity and strongly correlated phases in bilayer graphene twisted at a magic angle, causing the emergence of flat bands in the electronic structure, has further boosted the theoretical and experimental research on FB systems.

The physics of two-body bound states in the presence of a flat band has been recently explored theoretically in different contexts, including topological matter [17–20] and the link between the inverse effective mass of the bound state and the quantum metric of the single-particle states [21–23]. This

second direction is related to the more general question of understanding how transport and superconductivity can occur in a system with quenched kinetic energy [24–33]. By increasing the fermion-fermion attraction, the many-body system progressively transforms into a bosonic gas of diatomic molecules. The evolution from a Bardeen-Cooper-Schrieffer (BCS) state to a Bose-Einstein condensate (BEC), commonly referred to as the BCS-BEC crossover, has been investigated both theoretically and experimentally in single-band dispersive systems, going from superconductors [34] to atomic Fermi gases [35]. Recent theoretical works [36–38] have generalized the theory to two-band *continuous* models describing superfluid Fermi gases near an orbital Feshbach resonance, and a significant increase of the critical temperature T_c has been predicted when the lower band becomes shallow [39,40]. Transport in many-body bosonic flat-band systems has also been explored; see, for instance, [41–45].

In this work we study, in a unified framework, the influence of the multiband structure and the proximity to a flat band on pairing phenomena, going from the formation of molecules in vacuum to superconductivity in many-body fermionic systems. Our investigation is based on the attractive Fermi-Hubbard model on the one-dimensional (1D) sawtooth lattice (also known as triangular or Tasaki lattice), shown in Fig. 1(a). Its unit cell contains two lattice sites, called A and B; particles can hop between two B sites with rate t , while tunneling between A and B sites occurs at a rate t' . Two combinations of the tunneling rates are of special interest: (i) the FB point, corresponding to $t = t'/\sqrt{2}$, where the lower Bloch band becomes dispersionless, and (ii) $t = 0$, where the sawtooth lattice reduces to the linear chain, and the Hubbard

*giuliano.orso@u-paris.fr

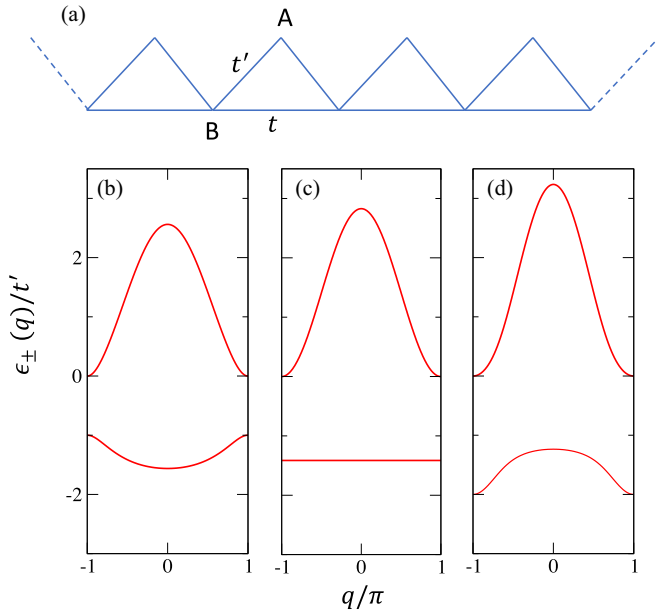


FIG. 1. (a) Geometry of the 1D sawtooth lattice. The lattice contains two sites per unit cell, indicated by A and B. We indicate by t' the hopping rate between A and B sites and by t the hopping rate between B sites. Notice that there is no tunneling between A sites. Panels (b)–(d) Dispersion relations of the two bands for different values of the tunneling ratio: $t/t' = 1/2$ (b), $t/t' = 1/\sqrt{2}$ (c), corresponding to the flat-band point, and $t/t' = 1$ (d). In this work, we fix the energy scale by setting $t' = 1$.

model is then integrable by the Bethe ansatz. We first present a thorough solution of the two-body problem, from which we extract the binding energy and the effective mass of the pair as a function of the tunneling rates t , t' and the Hubbard strength U . We then show that in many-body systems, the proximity to a flat band strongly modifies the nature of the superconducting state, as compared to the integrable limit. The chemical potential remains always closed to its zero-density limit, even in the weakly interacting regime. In contrast, the superfluid pairing gap is strongly depleted at finite density, and its peak is shifted with respect to the FB point. We explain this surprising effect by studying the change in the ground-state energy of the system upon adding an extra fermion. For nonzero t and $|U|$ sufficiently large, this quantity falls below the bottom of the single-particle energy spectrum, indicating that pairs and single fermions tend to attract each other. To support this picture, we explicitly show that three-body bound states do appear in the sawtooth lattice. We compute their binding energy E_b^{trimer} as a function of the interaction strength and the tunneling rates. We show that E_b^{trimer} exhibits a peak at the FB point, in complete analogy with the two-body case. Importantly, we use a strong-coupling variational approach to show that trimers originate from tunneling-induced exchange processes.

Superconductivity in the sawtooth lattice at the FB point has been recently investigated numerically in Ref. [30], with a focus on the superfluid weight D_s . The authors introduced a modified multiband BCS theory with sublattice-dependent order parameters to account for the different connectivity of the A and B sites. In this way, the mean-field approach was

shown to compare well with density matrix renormalization group (DMRG) calculations.

The article is organized as follows. In Sec. II we review the single-particle properties of the sawtooth lattice, and we present the formalism used to solve the two-body problem in a multiband lattice. In Sec. III we show our results for the binding and the effective mass of the two-body bound states, both at the FB point and for generic tunneling rates. In Sec. IV we present our DMRG results for the BCS-BEC crossover at finite density, while in Sec. V we discuss the formation of trimers in the sawtooth lattice. Finally, in Sec. VI we present our conclusions.

II. THEORETICAL APPROACH

A. Single-particle properties

We recall here the single-particle properties of the 1D sawtooth lattice, shown in Fig. 1(a). The tight-binding Hamiltonian is given by

$$H_{\text{sp}} = \sum_i t |i^B\rangle \langle i+1^B| + \text{H.c.} + t' |i^A\rangle \langle (i+1^B)| + \text{H.c.}, \quad (1)$$

with $|i^{A/B}\rangle$ denoting the local (site) basis. The dispersion relations of the two bands associated with the Hamiltonian (1) are given by

$$\epsilon_{\pm}(q) = t \cos q \pm \sqrt{t^2 \cos^2 q + 2t'^2(1 + \cos q)}, \quad (2)$$

where q is the wave vector of the Bloch state, and we have used the distance between two adjacent sites as length unit. In Fig. 1 [panels (b)–(d)], we show how the shapes of the two bands evolve as the tunneling ratio t/t' is changed. While the upper band is always concave down at $q=0$, the bottom $q=q_B$ of the lower band changes from $q_B=0$ for $t/t' < 1/\sqrt{2}$, to $q_B=\pi$ for $t/t' > 1/\sqrt{2}$. Exactly at $t/t' = 1/\sqrt{2}$, the lower band becomes flat, $\epsilon_-(q) = -\sqrt{2}t'$ [panel (c)], implying that the inverse effective mass $1/m^* = \epsilon''_-(q_B)$ vanishes. For any other value of t , Eq. (2) yields

$$\frac{1}{m^*} = \begin{cases} -t + \frac{t'^2 + t^2}{\sqrt{4t'^2 + t^2}} & \text{if } \frac{t}{t'} < \frac{1}{\sqrt{2}}, \\ -\frac{t^2}{t} + 2t & \text{if } \frac{t}{t'} > \frac{1}{\sqrt{2}}. \end{cases} \quad (3)$$

The amplitudes of the Bloch states at site j associated with the energy bands $\epsilon_v(q)$ can be conveniently written as $\Psi_{qv}(j) = \frac{e^{iqj}}{\sqrt{L}} (\alpha_{qv}, \beta_{qv})$, where L is the number of unit cells, while α_{qv}, β_{qv} satisfy

$$\alpha_{qv} = \frac{t'(1 + e^{-iq})}{\epsilon_v(q)} \beta_{qv}, \quad (4)$$

together with the normalization condition $|\alpha_{qv}|^2 + |\beta_{qv}|^2 = 1$. Since $\epsilon_v(-q) = \epsilon_v(q)$, we are free to choose β_{qv} real and satisfying $\beta_{-qv} = \beta_{qv}$. From Eq. (4) we then find that $\alpha_{-qv} = \alpha_{qv}^*$, where the star indicates the complex conjugate.

B. Two-body problem

We now consider two particles hopping on the sawtooth lattice and coupled by contact interactions. The two-body Hamiltonian is given by $\hat{H} = \hat{H}_0 + \hat{U}$, where

$\hat{H}_0 = \hat{H}_{\text{sp}} \otimes \mathbb{1} + \mathbb{1} \otimes \hat{H}_{\text{sp}}$ is the noninteracting Hamiltonian, and $\hat{U} = U(\hat{P}^A + \hat{P}^B)$ accounts for contact interactions between the two particles. Here $\hat{P}^\sigma = \sum_{m^\sigma} |m^\sigma m^\sigma\rangle \langle m^\sigma m^\sigma|$ are the pair projector operators over the doubly occupied sites of the $\sigma = A, B$ sublattices. The properties of two-body bound states can be obtained by mapping the stationary Schrödinger equation into an effective single-particle model for the center-of-mass motion of the pair, as was done in Refs. [46,47] for continuous and lattice models, respectively. If the external potential is periodic, the momentum Q of the pair is conserved, and the problem reduces further to finding the eigenvalues of an $N_b \times N_b$ matrix, where N_b is the number of basis sites per unit cell, as we shall see below for $N_b = 2$. The same equation was obtained recently by Iskin in Ref. [22] by using a different (variational) approach. Scattering states in flat bands have instead been discussed in [48], but they can also be obtained by adapting the formalism below, as was done in Ref. [49].

We start by writing the two-body Schrödinger equation as $(E - \hat{H}_0)|\psi\rangle = \hat{U}|\psi\rangle$, where E is the total energy of the pair. Substituting it into the Schrödinger equation and bringing the operator $(E - \hat{H}_0)$ on the right-hand side yields

$$\frac{1}{U}|\psi\rangle = (E - \hat{H}_0)^{-1}\hat{P}^A|\psi\rangle + (E - \hat{H}_0)^{-1}\hat{P}^B|\psi\rangle. \quad (5)$$

Next, by projecting the wave function (5) on the doubly occupied states $|m^\sigma m^\sigma\rangle$, we obtain a close equation for the corresponding amplitudes $f(n) = \binom{n^A n^A}{n^B n^B} |\psi\rangle$ as

$$f(n) \frac{1}{U} = \sum_m K(n, m) f(m), \quad (6)$$

where, for given values of n and m , $K(n, m)$ is a 2×2 matrix depending parametrically on the energy and whose entries are given by $K^{\sigma\sigma'}(n, m) = \langle n^\sigma n^\sigma | (E - \hat{H}_0)^{-1} | m^{\sigma'} m^{\sigma'} \rangle$. The latter can be conveniently expressed in terms of the components of the single-particle Bloch wave functions $\Psi_{q\lambda}(j)$, so that Eq. (6) takes the form

$$f(n) \frac{1}{U} = \frac{1}{L^2} \sum_{m, q, p, v, v'} \frac{e^{i(q+p)(n-m)}}{E - \varepsilon_v(q) - \varepsilon_{v'}(p)} M_{vv'}(q, p) f(m), \quad (7)$$

where

$$M_{vv'}(q, p) = \begin{pmatrix} \alpha_{qv} \alpha_{qv}^* \alpha_{pv'} \alpha_{pv'}^* & \alpha_{qv} \beta_{qv}^* \alpha_{pv'} \beta_{pv'}^* \\ \beta_{qv} \alpha_{qv}^* \beta_{pv'} \alpha_{pv'}^* & \beta_{qv} \beta_{qv}^* \beta_{pv'} \beta_{pv'}^* \end{pmatrix}. \quad (8)$$

One can easily see that the eigenstates of Eq. (7) are plane waves $f(n) = \frac{e^{iQn}}{\sqrt{L}} f_Q$, with Q being the center-of-mass momentum of the pair. By substituting it into Eq. (7) and taking the continuum limit, we end up with the eigenvalue problem

$$f_Q \frac{1}{U} = R f_Q, \quad (9)$$

$$R_{11} = \frac{8\sqrt{E(E-4\sqrt{2})} + E(16 + 2\sqrt{2}E - E^2 + 2\sqrt{2}\sqrt{E^2-2}) - \frac{12E(E+\sqrt{2})}{\sqrt{E^2-2}}}{E(32\sqrt{2} + 24E - E^3)},$$

$$R_{12} = R_{21} = \frac{2\left(\sqrt{2}\sqrt{-\frac{E(E^2-2)}{4\sqrt{2}-E}} + \sqrt{2}E + 2\right)}{(E + 2\sqrt{2})^2 \sqrt{E^2-2}}, \quad (13)$$

where $R = R(E, Q)$ is a 2×2 matrix defined as

$$R = \sum_{v, v'} \int_{-\pi}^{\pi} \frac{dq}{2\pi} \frac{M_{vv'}(q, Q-q)}{E - \varepsilon_v(q) - \varepsilon_{v'}(Q-q)}. \quad (10)$$

The two eigenvalues of the matrix R are given by

$$\lambda_{\pm} = \frac{R_{11} + R_{22}}{2} \pm \frac{1}{2} \sqrt{(R_{11} - R_{22})^2 + 4|R_{12}|^2}. \quad (11)$$

For a given interaction strength U and quasimomentum Q , the energy levels of bound states are obtained by looking for a solution of $\lambda_{\pm}(E, Q) = 1/U$, the energy E taking values outside the noninteracting two-body energy spectrum. In the following, we fix the energy scale by setting $t' = 1$, and we restrict to attractively bound states, corresponding to $U < 0$.

III. TWO-BODY RESULTS

A. Bound states at the FB point

We present here our results for the two-body bound states for the special case $t = 1/\sqrt{2}$, where the lower Bloch band becomes flat; see Fig. 1(c). We will be interested in the solutions of Eq. (9) with energy $E < E_{\text{ref}}$, where $E_{\text{ref}} = 2\epsilon_-(q_B) = -2\sqrt{2}$ is the ground-state energy of the two-body system in the absence of interactions. These states are often referred to as *doublons*, since for large $|U|$ the two particles sit at the same site and form a tightly bound molecule with energy $E \sim U$.

The integration over momentum in Eq. (10) will be generally performed numerically. Analytical integration is also possible via residue techniques, although the calculation can become difficult for arbitrary combinations of the parameters E and Q . As an example, we provide here the exact expression for the matrix R valid for zero center-of-mass momentum and $E < E_{\text{ref}}$. This allows us to extract the pair binding energy exactly for any $U < 0$. To this end, we substitute in Eq. (8) the amplitudes of the Bloch wave functions obtained from Eq. (4):

$$\alpha_{q-} = -\frac{1 + e^{-iq}}{\sqrt{2(2 + \cos q)}}, \quad \beta_{q-} = \frac{1}{\sqrt{2 + \cos q}}, \quad (12)$$

$$\alpha_{q+} = \frac{1 + e^{-iq}}{\sqrt{2(2 + \cos q)(1 + \cos q)}}, \quad \beta_{q+} = \sqrt{\frac{1 + \cos q}{2 + \cos q}},$$

and the corresponding dispersion relations of the two bands, with $\varepsilon_+(q) = \sqrt{2}(1 + \cos q)$. For $Q = 0$, the integration over momentum is performed by introducing the complex variable $z = e^{iq}$, so that the integrating function takes the form of a ratio $t(z)/y(z)$ of two analytical functions. We then calculate the integral via Cauchy's residue theorem of complex analysis, after identifying the poles inside the circle $|z| = 1$. This gives

$$R_{22} = \frac{2(\sqrt{2}E + 2)\sqrt{-E - \sqrt{2}} + E(E + \sqrt{2})\sqrt{\frac{E(2 - \sqrt{2}E)}{\sqrt{2}E - 8}}}{(E + 2\sqrt{2})\sqrt{\sqrt{2} - E}(E^2 + 3\sqrt{2}E + 4)}.$$

We substitute Eqs. (13) in Eq. (11) and obtain the exact energy of the bound state from the implicit condition $U = 1/\lambda_-(E)$ (notice that the eigenvalue λ_+ yields the energy of the first excited bound state). We then extract the binding energy E_b from the relation $E = -E_b + E_{\text{ref}}$, so that $E_b > 0$ if the state is bound. In Fig. 2 we plot our results for the binding energy as a function of the interaction strength (blue solid curve). We can use the exact relation between E and U to obtain the asymptotic expansions for the binding energy in the weak- and strong-coupling regimes. In the noninteracting limit, the binding energy vanishes, implying that $E = E_{\text{ref}} = -2\sqrt{2}$. For small U we perform a quadratic expansion of $1/\lambda_-(E)$ in powers of $E + 2\sqrt{2}$, yielding $U \simeq c_1(E + 2\sqrt{2}) + c_2(E + 2\sqrt{2})^2$, where $c_1 = (5 + 4\sqrt{3} - \sqrt{37 + 16\sqrt{3}})/2 \simeq 1.942$ and $c_2 = \frac{27[3 - 4\sqrt{3} + 2\sqrt{3(67 - 36\sqrt{3})}]}{\sqrt{134 - 72\sqrt{3}(9 - 2\sqrt{3} + \sqrt{3(67 - 36\sqrt{3})})^2}} \simeq 0.365$. The same result can also be obtained by noting that for small U the dominant contribution to the integral in Eq. (10) corresponds to $\nu = \nu' = -$, leading to a pole at $E = E_{\text{ref}}$ in the matrix elements of R , while in all the other contributions E can be safely replaced by E_{ref} . The binding energy of the pair in the weak-coupling regime is then given by

$$E_b \simeq -\frac{U}{c_1} + \frac{c_2}{c_1^3}U^2, \quad (14)$$

which is shown in Fig. 2 by the dot-dashed curve. Notice that the linear-in- U dependence of the binding energy for small U , also reported in [21], is a direct consequence of the localized

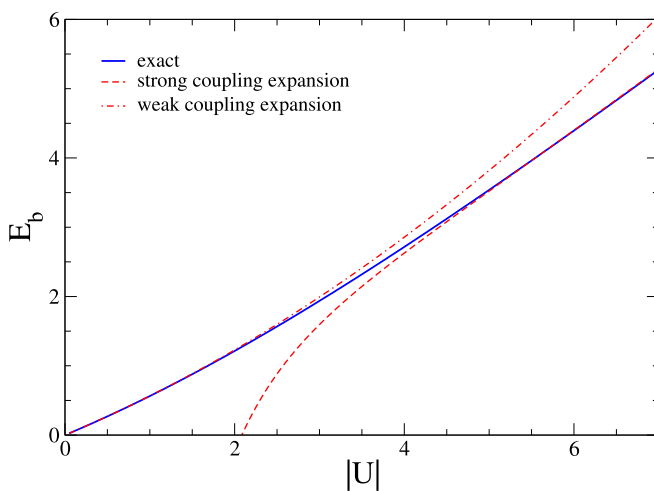


FIG. 2. Binding energy of the deepest two-body bound state at the flat-band point, $t = 1/\sqrt{2}$, plotted as a function of the modulus of the interaction strength (blue solid line). The dot-dashed line corresponds to the weak-coupling expansion, Eq. (14), while the dashed line represents the strong-coupling expansion, Eq. (15). We set $t' = 1$ as the energy unit.

nature of the single-particle states forming the molecule. Indeed, the same behavior was already observed [47] for two interacting particles in the presence of a quasiperiodic lattice once single-particle localization set in.

For strong interactions, we expand $\lambda_-(E)$ in power of $1/E$ up to second order. From this we find

$$E_b \simeq -U - 2\sqrt{2} - \frac{6 + 2\sqrt{5}}{U} - \frac{16\sqrt{2/5} + 6\sqrt{2}}{U^2}. \quad (15)$$

The strong-coupling expansion (15) is shown in Fig. 2 by the dashed curve, and it agrees well with the exact result for $|U| \gtrsim 5$. Before continuing, it is worth mentioning that the occupation of the two sublattices is asymmetric due to the different connectivity of A and B sites: in the bound state of lowest energy, the two constituent particles reside more on the B sublattice, while in the first excited bound state the two particles occupy predominantly the A sites. This point is particularly clear in the strong-coupling regime, since the two particles must share the same site to interact. Expanding the matrix elements in Eq. (13) to lowest order in $1/E$ yields

$$R = \begin{pmatrix} 1/E + 4/E^3 & 4/E^3 \\ 4/E^3 & 1/E + 8/E^3 \end{pmatrix}.$$

The eigenvalues of Eq. (16) are $\lambda_{\pm} = 1/E + (6 \mp 2\sqrt{5})/E^3$ and the associated normalized eigenvectors are, respectively, $\mathbf{v}_- = (v_1, v_2)$ and $\mathbf{v}_+ = (-v_2, v_1)$, where $v_1 = \sqrt{2/(5 + \sqrt{5})}$ and $v_2 = \sqrt{(5 + \sqrt{5})}/10$. Hence the probability for the pair to be in the A site is $|v_-^A|^2 = 0.276$ for the ground state and $|v_+^A|^2 = 0.724$ for the first excited bound state. This result is consistent with Ref. [30], also reporting an asymmetric occupation of the two sublattices for the ground-state density profile at finite filling.

Let us now discuss the effective mass m_p^* of the pair, which is defined through the relation $1/m_p^* = E''(0)$, where $E(Q)$ is the dispersion relation of the bound state. In Fig. 3 we plot the inverse effective mass of the pair as a function of the interaction strength (solid blue line). For $U = -0.1414$ we recover the numerical result obtained in Ref. [21]. To derive the weak-coupling expansion for the pair effective mass, we need to calculate the matrix R for a small but finite momentum Q . To do so, in Eq. (10) we perform a quadratic expansion in Q for the nonsingular contributions and replace therein the energy E by $-2\sqrt{2}$. The integration can then be performed analytically yielding the following approximate expressions

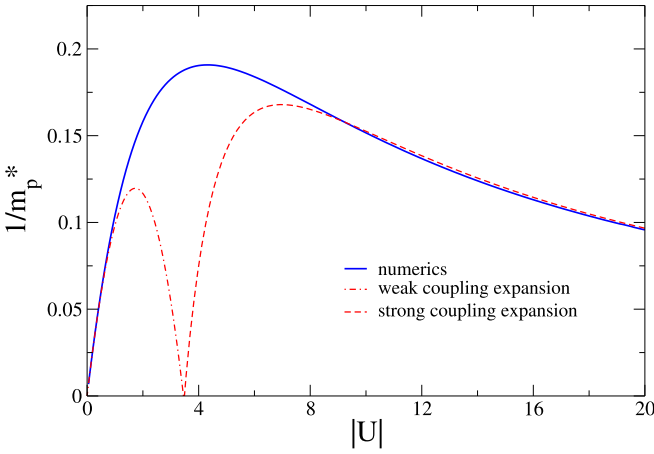


FIG. 3. Inverse effective mass of the deepest bound state at the flat-band point as a function of the modulus of the interaction strength. The dot-dashed line corresponds to the weak-coupling expansion, Eq. (17), while the dashed line represents the strong-coupling expansion, Eq. (27).

for the matrix elements:

$$\begin{aligned}
 R_{11} &\simeq \frac{(\sqrt{3}-2)(7-\cos Q)+4}{(7-\cos Q)\sqrt{3}(E+2\sqrt{2})} - \frac{1008+187Q^2}{1728\sqrt{6}}, \\
 R_{12} &\simeq \frac{2e^{-iQ/2}\cos(Q/2)}{(7-\cos Q)\sqrt{3}(E+2\sqrt{2})} + \frac{432-Q(185Q+i216)}{1728\sqrt{6}}, \\
 R_{22} &\simeq \frac{4}{(7-\cos Q)\sqrt{3}(E+2\sqrt{2})} - \frac{5(144+11Q^2)}{1728\sqrt{6}}. \quad (16)
 \end{aligned}$$

We then substitute the right-hand side of Eqs. (16) in (11) and expand $1/\lambda_- = U$ up to second order in $E+2\sqrt{2}$. We obtain $U \simeq f_1(Q)(E+2\sqrt{2}) + f_2(Q)(E+2\sqrt{2})^2$, where $f_i(Q) = c_i + d_i Q^2$ are quadratic functions of the momentum. The constant c_i is defined as above, while $d_1 = \frac{1}{8}(\sqrt{\frac{1}{601}(1504\sqrt{3}+3133)} - 1) \simeq 0.261$ and $d_2 = \frac{6}{\sqrt{2}}(\frac{148042277-85446942\sqrt{3}}{\sqrt{67-36\sqrt{3}}}-5341612+3094257\sqrt{3}) \simeq 0.294$. Solving for the energy yields $E(Q) \simeq -2\sqrt{2} + \frac{U}{f_1(Q)} - \frac{f_2(Q)}{f_1(Q)^2}U^2$. The effective mass of the pair is then given by

$$\frac{1}{m_p^*} \simeq -\frac{2d_1}{c_1^2}U + \frac{6c_2d_1 - 2d_2c_1}{c_1^4}U^2, \quad (17)$$

which is displayed in Fig. 3 with the dot-dashed red line. We see that the inverse effective mass takes its maximum value around $U = -4.3$. Interestingly, there is a wide window of U values around this point, where both the perturbative expansion (17) and the strong-coupling expansion, which will be derived below [see Eq. (27)], become completely inadequate. In particular, the pair effective mass is much more sensitive to interband transitions than the binding energy, as one can see by comparing Fig. 3 with Fig. 2.

The dependence of $1/m_p^*$ on $|U|$ shown in Fig. 3 is clearly reminiscent of the behavior of the superfluid weight D_s investigated in [30]: both quantities scale as $|U|$ for weak interactions and as $1/|U|$ in the strongly interacting regime. For small $|U|$, the explicit relation between the pair effective

mass and the superfluid weight is [50] $D_s = 4\pi n(1-n)/m_p^*$, where n is the density (i.e., the number of fermions per lattice site), and the factor π has been added to match the definition of D_s used in [30]. In this regime, Eq. (17) yields $1/m_p^* \simeq 0.1385|U|$, implying $D_s \simeq 1.74|U|n(1-n)$, which is close to the value $D_s \simeq 1.62|U|n(1-n)$ found in [30] from DMRG data at quarter filling, $n = 1/4$.

It is also worth emphasizing that the linear-in- U behavior of the pair inverse effective mass for small U is a generic feature of FB lattices. Indeed, in this regime the matrix R in Eq. (10) takes the approximate form $R \simeq W/(E-2\varepsilon_{\text{fb}})$, where ε_{fb} is the energy of the flat band and W is a Q -dependent matrix given by

$$W = \begin{pmatrix} \sum_q |\alpha_q|^2 |\alpha_{Q-q}|^2 & \sum_q \alpha_q \beta_q^* \alpha_{Q-q} \beta_{Q-q}^* \\ \sum_q \alpha_q^* \beta_q \alpha_{Q-q}^* \beta_{Q-q} & \sum_q |\beta_q|^2 |\beta_{Q-q}|^2 \end{pmatrix} \quad (18)$$

with α_k, β_k being the amplitude components of the FB states. Therefore, the energy dispersion of the weakly bound state is $E(Q) = 2\varepsilon_{\text{fb}} + U\lambda_W(Q)$, where $\lambda_W(Q) = (W_{11} + W_{22} + \sqrt{(W_{11} - W_{22})^2 + 4|W_{12}|^2})/2$ corresponds to the largest positive eigenvalue of W . In particular, the inverse effective mass of the pair is given by $1/m_p^* = U\partial^2\lambda_W/\partial Q^2$ evaluated at $Q = 0$. Notice that this result is completely general, i.e., it does not depend on any assumption of uniform pairing across the two sublattices.

B. Bound states for generic tunneling rates

We investigate here the properties of the lowest energy bound state in the absence of the flat band, i.e., for an arbitrary $t \neq 1/\sqrt{2}$. From Eq. (2) we find that the reference energy is given by

$$E_{\text{ref}} = \begin{cases} 2(t - \sqrt{4+t^2}) & \text{if } t < \frac{1}{\sqrt{2}}, \\ -4t & \text{if } t > \frac{1}{\sqrt{2}}. \end{cases} \quad (19)$$

This quantity exhibits a maximum with discontinuous derivative at the FB point, due to the crossing between the two defining functions in Eq. (19). In Fig. 4 we plot the binding energy as a function of the tunneling rate t for different values of U (solid lines). The two panels (a) and (b) correspond to the weak- and strong-coupling regimes, respectively. We see that E_b takes its maximum value in correspondence of the FB point (solid vertical line) for all values of the interaction strength. The origins of the peak in the weak and in the strongly interacting regimes are different. In the first case, it directly follows from the fact that at the FB point E_b scales linearly in U , while for any other values of t the binding energy grows only quadratically in U . To see this, we perform a quadratic expansion around the bottom of the lower band, $\epsilon_-(q) \simeq \epsilon_-(q_B) + \epsilon''_-(q_B)(q-q_B)^2/2$. Next, we approximate the numerator on the right-hand side of Eq. (10) by a constant, $M_{--}(q, -q) \simeq M_{--}(q_B, -q_B)$, and we integrate over momentum. From Eq. (11) we obtain

$$\frac{1}{U} \simeq -\frac{(|a_{q_B}|^4 + |b_{q_B}|^4)}{2\sqrt{\epsilon''_-(q_B)}\sqrt{E_b}}, \quad (20)$$

showing that for small U the binding energy grows as U^2 . This behavior is well known from the linear chain limit $t = 0$, where $E_b = \sqrt{U^2 + 16} - 4$. Equation (20) breaks down for

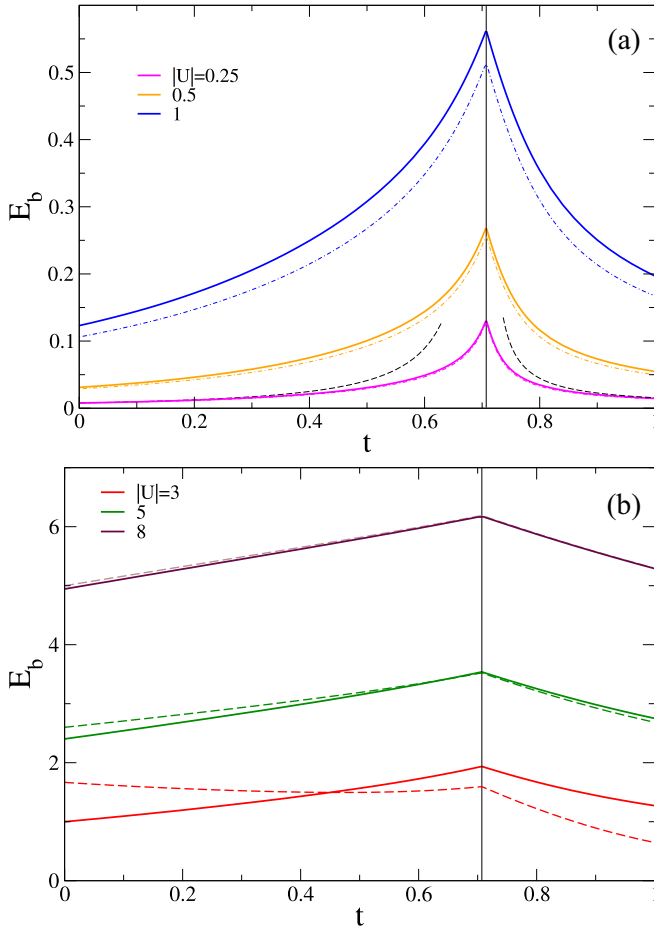


FIG. 4. (a) Binding energy vs tunneling rate for different values of U in the weakly interacting regime, from $U = -0.25$ (bottom) to $U = -1$ (top), shown with solid lines. The dot-dashed curves correspond to the single-band approximation obtained by retaining only the contribution from the lower band in Eq. (10). The dashed line corresponds to the weak-coupling result $E_b = U^2 f$, where the function $f(t)$ is defined in Eq. (21). Notice that f diverges approaching the flat-band point $t = 1/\sqrt{2}$ (vertical line). (b) Same as panel (a) but for values of U in the strongly interacting regime, from $U = -3$ (bottom) to $U = -8$ (top), shown with solid lines. The dashed lines correspond to the strong-coupling expansion, Eq. (23). Notice that the binding energy takes its maximum value at the flat-band point for any value of U .

$t = 1/\sqrt{2}$, since the single-particle inverse effective mass vanishes at the FB point. We therefore write $E_b \simeq U^2 f(t)$, where

$$f(t) = \begin{cases} -\frac{(2+t^2)^2 \sqrt{4+t^2} (2+t^2 - t \sqrt{4+t^2})^2}{(4+t^2 - t \sqrt{4+t^2})^4 [-1 + t(-t + \sqrt{4+t^2})]} & \text{if } t < \frac{1}{\sqrt{2}}, \\ \frac{t}{8t^2 - 4} & \text{if } t > \frac{1}{\sqrt{2}} \end{cases} \quad (21)$$

is a function of the tunneling rate, which is obtained by substituting in Eq. (20) the explicit expressions for the effective mass and the amplitudes of the Bloch states, given in Eqs. (3) and (4), respectively. In Fig. 4(a) we display the result based on Eq. (21) for the weakest interaction considered, $U = -0.25$ (dashed line). We see that there is a wide region of t values around the FB point, where the weak-coupling approximation (20) deviates significantly from the numerical

result. We emphasize that Eq. (20) relies on the assumption that $E_b \ll w$, where $w = |\sqrt{4+t^2} - 3t|$ is the width of the lowest-energy band. This condition is necessarily violated near the FB point, where the bandwidth vanishes.

The dot-dashed curve in Fig. 4(a) refers to the single-band approximation for the binding energy, obtained by neglecting completely the upper band in Eq. (10), thus retaining only the contribution corresponding to $\nu = \nu' = -$. For weak interactions, the approximation is accurate for any value of t , in stark contrast with the weak-coupling expansion (20), pointing out that all momenta inside the Brillouin zone must be taken into account when approaching the FB point. As $|U|$ increases, interband transitions become important and the single-band approximation deviates more and more from the exact numerics.

In the presence of a very strong attraction, the two particles sit at the same lattice site and form a tightly bound state. Since $E \sim U$ is large and negative, the binding energy reduces to $E_b \simeq -U + E_{\text{ref}}$. Thus, in this regime the binding energy simply mirrors the reference energy, showing a singular peak for $t = 1/\sqrt{2}$, as displayed in Fig. 4(b). To include higher-order corrections to the binding energy, we use the formula $\frac{1}{(E-x)} = \frac{1}{E} \sum_{n=0}^{+\infty} (\frac{x}{E})^n$ on the right-hand side of Eq. (10), with $x = \varepsilon_\nu + \varepsilon_{\nu'}$, and we cut the series after the $n = 3$ term. The integration over momentum can then be done analytically, and from Eq. (11) we obtain

$$\frac{1}{U} \simeq \frac{E^3 + 12t + 4E(1+t^2)}{E^4} \frac{4\sqrt{13t^2 + E(6t + 4t^3)} + E^2(1+t^4)}{E^4}. \quad (22)$$

Expanding the right-hand side of Eq. (22) in powers of E , up to second order, gives $U \simeq E + a_1/E + a_2/E^2$, where $a_1 = -4(1+t^2 + \sqrt{1+t^4})$ and $a_2 = -12t - (12t + 8t^3)/\sqrt{1+t^4}$. From this we obtain

$$E_b \simeq -U + E_{\text{ref}} - \frac{a_1}{U} - \frac{a_2}{U^2}, \quad (23)$$

which reduces to Eq. (15) for $t = 1/\sqrt{2}$. The strong-coupling prediction (23) is displayed in Fig. 4(b) with dashed lines. We see that the approximation works better and better as $|U|$ increases.

Let us now discuss the behavior of the two-body inverse effective mass. In Fig. 5 we display our numerical results as a function of the tunneling rate t and for different values of the interaction strength. The dotted line corresponds to the noninteracting limit, where the bound state breaks down and the pair effective mass reduces to twice the single-particle mass, $m_p^* = 2m^*$. We see that, far from the FB point, weak interactions tend to slightly increase the effective mass of the pair. In contrast, close to it, the inverse mass is strongly enhanced by interactions, an effect that persists until $U \approx -5$. We also note that the minimum in the inverse effective mass shifts towards smaller values of t as $|U|$ increases.

The interaction correction to $1/m_p^*$ in the weak-coupling regime can be obtained by generalizing Eq. (20) to a finite momentum of the pair. In particular, for $Q > 0$ the dominant contribution to the integral in Eq. (10) comes from the region centered around $q = q_B + Q/2$, with q_B defined as above. By

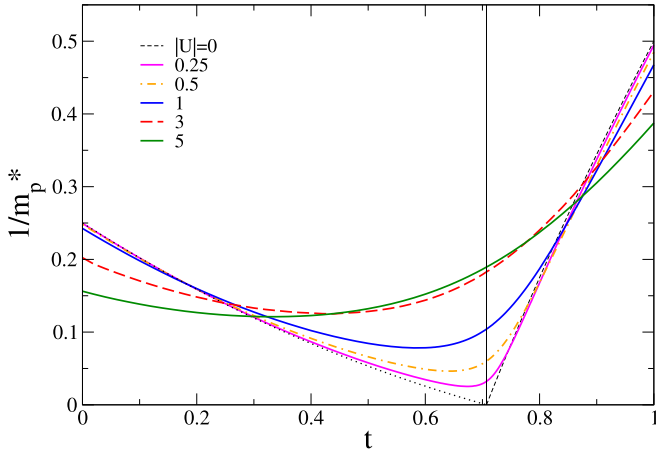


FIG. 5. Inverse effective mass of the deepest bound state as a function of the tunneling rate t for different values of the interaction strength $U = -0.25$ (magenta solid line), $U = -0.5$ (orange dot-dashed line), $U = 1$ (blue solid line), $U = -3$ (red long dashed line), and $U = -5$ (green solid line). The dotted line corresponds to the limit of vanishing attractive interactions, $m_p^* = 2m^*$. The vertical line represents the flat-band point $t = 1/\sqrt{2}$.

replacing q_B with $q_B + Q/2$ in Eq. (20) and taking the square of both sides of the equation, we obtain the dispersion relation

$$\frac{1}{U} \simeq \frac{1}{E^4} \{E(4 + E^2) + 6t(1 + \cos Q) + 2Et^2(1 + \cos Q) - \sqrt{8(E + 3t)^2(1 + \cos Q) + 4t^2[1 + Et + (3 + Et)\cos Q]}\}, \quad (26)$$

which provides an implicit equation for the dispersion relation of the bound state. To make it explicit, we expand the right-hand side of Eq. (26) in powers of $1/E$, retaining up to second-order terms, and we solve for the energy. This yields

$$\frac{1}{m_p^*} \simeq -\frac{1 + 2t^2(t^2 + \sqrt{1 + t^4})}{U\sqrt{1 + t^4}} - \frac{t(3 + 8t^2 + 6t^6 + 6\sqrt{1 + t^4} + 6t^4\sqrt{1 + t^4})}{U^2(1 + t^4)^{3/2}}, \quad (27)$$

holding for any value of t , including the FB point (see the dashed curve in Fig. 3). Notice that the $1/U^2$ correction in Eq. (27) accounts for the nonmonotonic behavior of the inverse effective mass displayed in Fig. 5, including the shift of the minimum towards smaller values of t as interaction effects become stronger.

IV. BCS-BEC CROSSOVER

In this section, we use the DMRG method to investigate the ground-state properties of a spin-1/2 Fermi gas on the sawtooth lattice undergoing the BCS-BEC crossover. The underlying Fermi-Hubbard Hamiltonian is given by

$$H = \sum_{i\alpha} [t c_{i\alpha}^{B\dagger} c_{i+1\alpha}^B + t' c_{i\alpha}^{A\dagger} (c_{i\alpha}^B + c_{i+1\alpha}^B) + \text{H.c.}] + U \sum_i (n_{i\uparrow}^A n_{i\downarrow}^A + n_{i\uparrow}^B n_{i\downarrow}^B), \quad (28)$$

of the bound state,

$$E(Q) = 2\epsilon_-(q_B + Q/2) - \frac{(|a_{q_B+Q/2}|^4 + |b_{q_B+Q/2}|^4)^2}{4\epsilon_-''(q_B + Q/2)} U^2. \quad (24)$$

From Eq. (24) we then find that the effective mass of the pair in the weak-coupling regime reduces to

$$\frac{1}{m_p^*} \simeq \frac{1}{2m^*} + hU^2, \quad (25)$$

where h is a function of the tunneling rate, whose explicit form is obtained by making use of Eqs. (2) and (4) in Eq. (24). We find $h(t) = \frac{4-t(8u+t\{60+t[40u+t(86+t\{25u+t[36+5t(t+u)])\}])}{16u^5(2t^2-1)}$ for $t < 1/\sqrt{2}$, with $u = \sqrt{4 + t^2}$, while $h(t) = (1 + t^2)/[16t(1 - 2t^2)]$ for $t > 1/\sqrt{2}$. Notice that h diverges for $t = 1/\sqrt{2}$, since in Eq. (24) $\epsilon_-''(q) = 0$ in the entire Brillouin zone. The divergence signals that Eq. (25) does not hold at the FB point, in agreement with Eq. (17).

The strong-coupling expansion for the pair effective mass can be obtained by following the same procedure used to derive Eq. (22), but this time we retain the full Q dependence of the matrix elements on the right-hand side of Eq. (10). The integration can still be performed analytically, and from Eq. (11) we obtain

where $c_{i\alpha}^{\sigma\dagger}$ ($c_{i\alpha}^\sigma$) is the local creation (annihilation) operator for fermions with spin component $\alpha = \uparrow, \downarrow$ in the sublattice $\sigma = A, B$, and $n_{i\alpha}^\sigma = c_{i\alpha}^{\sigma\dagger} c_{i\alpha}^\sigma$ are the corresponding density operators. We recall that $t' = 1$ in our energy units. We define the density of the two spin components with respect to the total number of lattice sites, $n_\alpha = N_\alpha/(2L)$, where N_α is the number of fermions with spin α . In this work, we restrict our attention to fully paired systems, corresponding to equal densities of the two spin components, and we assume that only the flat band is occupied in the absence of interactions, that is, $n_\uparrow = n_\downarrow < 1/2$.

Two important observables characterizing the BCS-BEC crossover in Fermi gases are the pairing gap Δ_{pg} and the chemical potential μ . The first, also known as the spin gap, corresponds to the energy needed to break a pair in the many-body system by reversing one spin, while the second corresponds to half the energy change upon adding a pair (one fermion with spin up and one fermion with spin down) to the system. Let $\epsilon(n, s)$ be the ground-state energy per lattice site, expressed in terms of the total fermion density $n = n_\uparrow + n_\downarrow$, and the spin density $s = n_\uparrow - n_\downarrow$. The pairing gap and the chemical potential are given by

$$\mu = \left(\frac{\partial \epsilon}{\partial n} \right)_{s=0}, \quad \Delta_{\text{pg}} = 2 \left(\frac{\partial \epsilon}{\partial s} \right)_{s=0}. \quad (29)$$

We compute the ground-state energy $E(N_\uparrow, N_\downarrow)$ of the system as a function of the spin populations N_α for a large enough

system size L . We consider system sizes up to $L = 60$, corresponding to 120 sites, with open boundary conditions.

We evaluate the chemical potential by approximating the derivative in Eq. (29) by a finite difference, $\mu \simeq [E(N_\uparrow + 1, N_\downarrow + 1) - E(N_\uparrow, N_\downarrow)]/2$. For the pairing gap, we use $-\Delta_{\text{pg}} \simeq E(N_\uparrow + 1, N_\downarrow + 1) - 2E(N_\uparrow + 1, N_\downarrow) + E(N_\uparrow, N_\downarrow)$. In the thermodynamic limit, this formula is equivalent to the finite difference $\Delta_{\text{pg}} \simeq E(N_\uparrow + 1, N_\downarrow - 1) - E(N_\uparrow, N_\downarrow)$, but it is less sensitive to finite-size effects. For vanishing densities, both the pairing gap and the chemical potential possess a well-defined limit, which is consistent with the solution of the two-body problem. The pairing gap reduces to the binding energy, since for $N_\uparrow = N_\downarrow = 0$ we find from Eq. (29) that $\Delta_{\text{pg}} = E(2, 0) - E(1, 1) = E_b$. Here we use the fact that $E(2, 0) = 2E(1, 0) = E_{\text{ref}}$ and $E(1, 1) = E(Q = 0)$, where $E(Q)$ is the energy dispersion of the two-body bound state calculated in Sec. III. From Eq. (29) we instead find that $\mu = E(1, 1)/2$, since $E(0, 0) = 0$, implying that the chemical potential reduces to

$$\mu = \frac{-E_b + E_{\text{ref}}}{2}. \quad (30)$$

A peculiar feature of 1D fermionic systems is that interaction effects become stronger as the density n decreases. As a consequence, the binding energy provides an upper bound for the pairing gap. In contrast, the two-body prediction (30) is a lower bound for the chemical potential, because the inverse compressibility $\partial\mu/\partial n$ must be positive or null to ensure the energetic stability of the gas.

Before presenting our results, we emphasize that the pairing gap discussed here is different from the pairing order parameters Δ^σ investigated in Ref. [30]. The latter are defined in terms of the diagonal part of the sublattice-resolved pair-pair correlation function through the relation $|\Delta^\sigma|^2/U^2 = \sum_i (\langle c_{i\uparrow}^\sigma c_{i\downarrow}^\sigma c_{i\downarrow}^\sigma c_{i\uparrow}^\sigma \rangle - \langle n_{i\uparrow}^\sigma \rangle \langle n_{i\downarrow}^\sigma \rangle)/L$. These quantities clearly depend on the many-body wave function and can therefore take different values on the two sublattices, $\Delta^A \neq \Delta^B$, due to the different connectivity of A and B sites. In contrast, the pairing gap is obtained solely from the ground-state energy of the system through Eq. (30) and therefore it cannot depend on the sublattice index. It is also worth adding that in Ref. [30] the pairing parameters Δ^σ are shown to be increasing functions of the density, while the pairing gap discussed here exhibits the opposite behavior [see Fig. 8(b) below]. Notice that the same difference in the density dependence of the two observables is also present in the linear chain limit $t = 0$; see, for instance, [51].

A. Results at the flat-band point

In Fig. 6 we plot the chemical potential versus $|U|$ at the FB point, together with the zero-density prediction (30). For weak enough interactions, finite density corrections are small, due to the infinite compressibility associated with the flat band. From Eqs. (14) and (30) we obtain, to first order in U , $\mu \simeq -\sqrt{2} + U/(2c_1)$, which is fully consistent with our numerics. This result differs from the BCS mean-field estimate given in [30], where the linear-in- U correction to

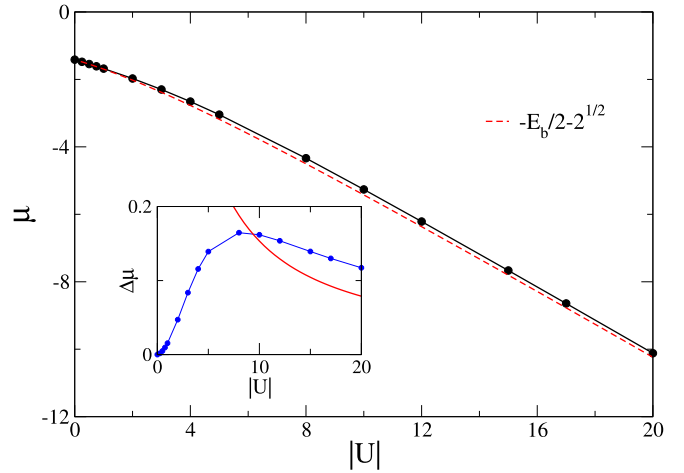


FIG. 6. Chemical potential at the flat-band point as a function of the modulus of the interaction strength for filling $n_\uparrow = n_\downarrow = 1/3$ (black circles). The dashed line represents the zero-density limit of the chemical potential, $\mu(n=0) = -E_b/2 + E_{\text{ref}}/2$; see Eq. (30). The data symbols in the inset correspond to the difference $\Delta\mu = \mu - \mu(n=0)$, plotted as a function of $|U|$. The red solid curve shows the corresponding result for $t = 0$, obtained from the Bethe ansatz integral equations, where $\Delta\mu = 1$ in the noninteracting limit. The solid connecting lines are a guide to the eye.

the chemical potential was found explicitly to depend on the density.

In the inset of Fig. 6 we plot the difference between the two curves in the main panel, corresponding to $\Delta\mu = \mu - \mu(n=0)$. This quantity shows a nonmonotonic behavior as a function of $|U|$: $\Delta\mu = 0$ in the absence of interactions, then it increases with $|U|$, reaching a maximum around $|U| \approx 8$, and finally it decreases as $\Delta\mu \sim 1/|U|$ in the strong-coupling regime. Notice that $\Delta\mu \geq 0$, because the inverse compressibility $(\partial\mu/\partial n)_{s=0}$ must be positive or zero to ensure the mechanical stability of the system. For large $|U|$, bound states behave as pointlike hard-core bosons, hopping between neighboring sites of the sawtooth lattice and experiencing repulsive nearest-neighbor interactions as well as a uniform potential of different strength in the two sublattices. Since all these processes are characterized by the same energy scale $1/U$, as demonstrated in Ref. [34], the leading density correction to Eq. (30) must be of the same order. For comparison, in the inset of Fig. 6 we also show the corresponding result for the integrable point $t = 0$ (red solid curve). This is obtained by solving numerically the Bethe ansatz integral equations, as was done in Ref. [52]. Differently from the FB case, at the integrable point $\Delta\mu$ is a monotonic decreasing function of $|U|$. In particular, $\Delta\mu = 1$ for $U = 0$ (because $n = 2/3$), while in the strong-coupling regime we find $\Delta\mu \sim 1/|U|$.

In Fig. 7 we show the pairing gap as a function of the modulus of the interaction strength (black circles), together with the two-body binding energy (red dashed line). For weak interactions, the numerical data are well fitted by $\Delta_{\text{pg}} = 0.44|U|$, shown by the blue dot-dashed line. For strong interactions, the difference between the binding energy and the pairing gap saturates to a constant value, as shown in the inset of Fig. 7. For comparison, in the inset we also display the

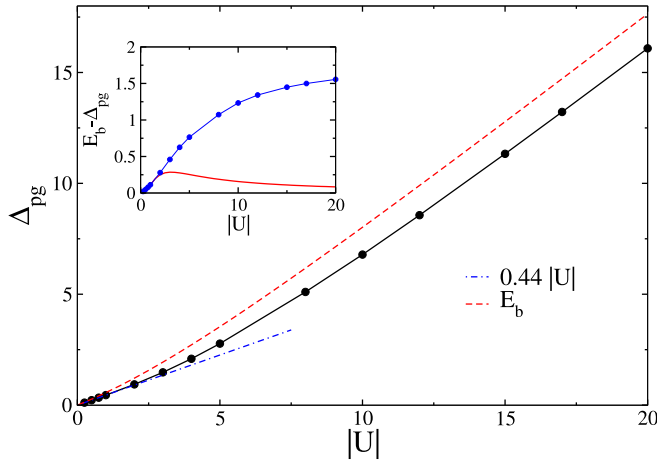


FIG. 7. Pairing gap at the flat-band point as a function of the modulus of the interaction strength, for filling $n_\uparrow = n_\downarrow = 1/3$ (black circles). The dashed line represents the zero-density limit of the pairing gap, $\Delta_{\text{pg}}(n=0) = E_b$. The data symbols in the inset correspond to the difference $E_b - \Delta_{\text{pg}}$, plotted as a function of $|U|$. The red solid line is the corresponding prediction for $t=0$, obtained from the Bethe ansatz integral equations, showing that the difference instead vanishes as $1/|U|$ for strong interactions. The connecting solid lines are a guide to the eye.

corresponding prediction for $t=0$ (red solid line), showing that the difference is instead nonmonotonic and decreases as $1/|U|$ in the strong-coupling regime.

The chemical potential and the pairing gap at the FB point show very different behaviors as a function of the density, as outlined in Fig. 8 [panels (a) and (b)] for $U = -15$. While the chemical potential is nearly constant for small n , the pairing gap decreases very rapidly at low densities ($n \lesssim 0.08$), suggesting a singular (i.e., nonanalytic) behavior for $n=0$. Moreover, finite-density effects are typically one order of magnitude larger for the pairing gap than for the chemical potential. The above results strongly contrast with the known

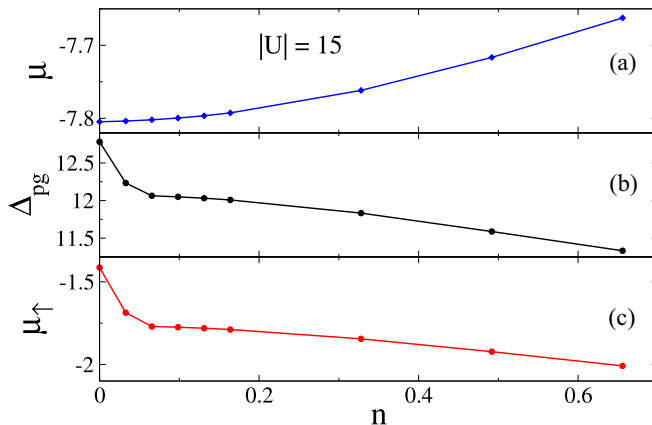


FIG. 8. Chemical potential (a), pairing gap (b), and excess energy (c) at the flat-band point as a function of the total fermion density n for $U = -15$. The solid connecting lines are a guide to the eye.

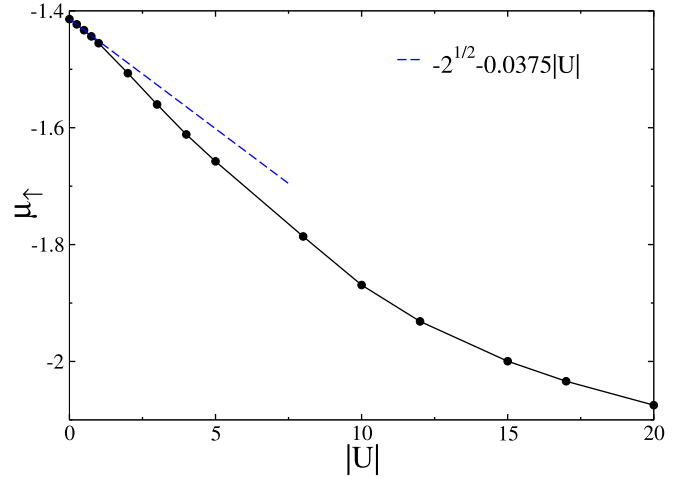


FIG. 9. Excess energy μ_\uparrow (see the text for definition) at the flat-band point as a function of $|U|$ for filling $n_\uparrow = n_\downarrow = 1/3$ (black circles). The blue dashed line represents the asymptotic behavior for weak interactions. The connecting line is a guide to the eye.

behavior at the integrable point $t=0$, where [53]

$$\mu = -\frac{\sqrt{U^2 + 16}}{2} + \frac{\pi^2 n^2}{4\sqrt{U^2 + 16}},$$

$$\Delta_{\text{pg}} = E_b - \frac{\pi^2 n^2}{2\sqrt{U^2 + 16}}, \quad (31)$$

which is valid for $n \ll 1$ and $|U| \gg 1$, with $E_b = \sqrt{U^2 + 16} - 4$. From Eqs. (31) we infer that density corrections are of the same order ($1/|U|$) for both quantities, and no singular behavior occurs at zero density.

To better understand the origin of the strong finite-density effects on the pairing gap, we study the *excess energy* μ_\uparrow , corresponding to the change in the ground-state energy of the system upon adding an extra spin-up fermion, $\mu_\uparrow = E(N_\uparrow + 1, N_\downarrow) - E(N_\uparrow, N_\downarrow)$. From Eq. (29) we find that this quantity is related to the previous observables by the general equation

$$\mu_\uparrow = \mu + \Delta_{\text{pg}}/2, \quad (32)$$

holding for any tunneling rate t and interaction strength U . From Eq. (32) we then find

$$\Delta_{\text{pg}} = E_b - E_{\text{ref}} + 2\mu_\uparrow - 2\Delta\mu, \quad (33)$$

implying that the density dependence of the pairing gap comes not only from the equation of state, as in Eqs. (31), but also from the excess energy. This point is particularly clear in Fig. 8(c), where μ_\uparrow is plotted as a function of the density, showing that the excess energy is responsible for the anomalous behavior of the pairing gap at low density.

In Fig. 9 we plot the excess energy as a function of the interaction strength. We see that μ_\uparrow is a decreasing function of $|U|$. For a noninteracting gas, $\mu_\uparrow = \mu = \epsilon_F = -\sqrt{2}$, since for $n < 1$ the upper dispersive band is empty. To first order in U we find $\mu_\uparrow \simeq -\sqrt{2} + UF(n)$, where $F(n)$ is a function of the density, satisfying $F(n=0) = 0$. This behavior is shown in Fig. 9 by the blue dashed line for $n = 2/3$. From Eq. (33) we then find, to the same order, that $\Delta_{\text{pg}} \simeq U(2F(n) - 1/c_1)$ since $\Delta\mu \simeq 0$. For large $|U|$, the excess energy does not

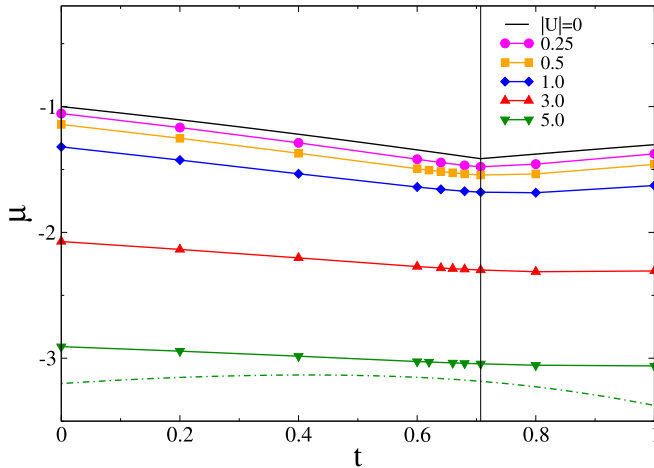


FIG. 10. Chemical potential μ as a function of the tunneling rate t plotted for different values of $U = 0, -0.25, -0.5, -1, -3, -5$ with $n_\uparrow = n_\downarrow = 1/3$. The two-body limit $\mu = (-E_b + E_{\text{ref}})/2$ for $U = -5$ is shown with the dot-dashed line. The vertical solid line indicates the flat-band point $t = 1/\sqrt{2}$. The connecting lines are a guide to the eye.

scale linearly with U , as the chemical potential does, because adding an extra fermion to a fully paired system does not change the number of pairs. Instead it saturates to a density-dependent value, which sits well below the energy of the flat band for the chosen density, $\mu_\uparrow < E_{\text{ref}}/2$. From Eq. (33) this implies that the pairing gap is strongly reduced by the finite density, as shown in the inset of Fig. 7, while corrections from the equation of state are subleading, since $\Delta\mu \sim 1/|U|$.

It is interesting to note that for strong interactions, Eq. (33) reduces to $\Delta_{\text{pg}} \simeq -E(1, 1) + 2\mu_\uparrow$, showing that the pairing gap yields the ground-state energy of the pair in vacuum, but measured with respect to the *many-body* reference energy $2\mu_\uparrow$, instead of the reference energy E_{ref} . In particular, the condition $\mu_\uparrow < E_{\text{ref}}/2$ indicates that the excess fermion and tightly bound pairs tend to attract each other, possibly leading to the formation of three-body bound states, as discussed in Sec. V below. We stress that this effective attraction is instead absent at the integrable point $t = 0$, since for large $|U|$, Eqs. (31) and (32) yield $\mu_\uparrow = -2 = E_{\text{ref}}/2$.

B. Results for the generic tunneling rate

In Fig. 10 we plot the chemical potential as a function of the tunneling rate for a fixed total density $n = 2/3$; the different curves correspond to different values of $|U|$. In the noninteracting limit (black solid line), the chemical potential coincides with the Fermi energy ε_F of the system, implying that $\mu = \varepsilon_-(q_B - \pi n/2)$. The curve exhibits a minimum at the FB point, due to the moderately large value of the density. In the presence of interactions, however, this minimum progressively disappears and the chemical potential flattens out because $\mu \approx U/2$ for large $|U|$. In Fig. 10 we also display the zero-density limit (30) of the chemical potential for $U = -5$. We see that the system is more compressible at $t \approx 0.6$.

In Fig. 11 we plot the ratio $\Delta_{\text{pg}}/|U|$ between the spin gap and the modulus of the interaction strength as a function of

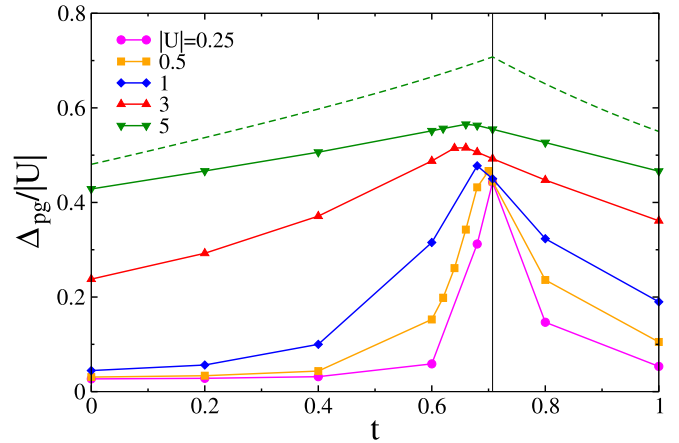


FIG. 11. Ratio between the pairing gap and $|U|$, plotted as a function of the tunneling rate t for different values of $U = -0.25, -0.5, -1, -3, -5$ with $n_\uparrow = n_\downarrow = 1/3$. The two-body binding energy E_b for $U = -5$ is shown for reference (dashed line). The vertical solid line indicates the flat-band point $t = 1/\sqrt{2}$. The connecting lines are a guide to the eye.

the tunneling rate t for increasing values of $|U|$. The obtained results are clearly similar to their two-body counterpart, presented in Fig. 4, showing a drastic enhancement of pairing in the vicinity of the FB point for weak to moderate interactions. There are other interesting and unexpected effects brought about by the finite density. First, the position of the maximum of the pairing gap drifts to smaller values of t as $|U|$ increases, while the two-body binding energy always remains peaked at $t = 1/\sqrt{2}$ (see Fig. 4). Second, for strong interactions density corrections are more prominent near the FB point, as can be seen in Fig. 11, where we contrast the pairing gap with the binding energy (dashed line) for $U = -5$. By comparing Fig. 10 with Fig. 11, we also see that density corrections for the chemical potential can be significantly smaller than for the pairing gap, except in a neighborhood of the integrable point $t = 0$, where Eqs. (31) apply.

In Fig. 12 we plot the corresponding results for the excess energy as a function of the tunneling rate. Far from the FB point, weak interactions cause a fast decrease of μ_\uparrow with respect to the Fermi energy, while near the FB point the decrease is rather modest. As a consequence, a local maximum appears, drifting towards smaller values of t as $|U|$ increases and turning into a global maximum at $t \approx 0.66$. Since for finite interactions the chemical potential in Fig. 10 depends smoothly on the tunneling rate, we find from Eq. (32) that the drift of the peak in the pairing gap simply reflects the behavior of the excess energy. As $|U|$ increases, we see from Fig. 12 that there is a growing window of t values around the FB point, in which the condition $\mu_\uparrow < E_{\text{ref}}/2$ is satisfied. In this region, the pairing gap is density-depleted for arbitrarily large $|U|$, as shown in Fig. 11. The anomalous attraction between Cooper pairs and extra fermions is therefore not specific to the FB point, but it appears as a general feature of multiband lattices as opposed to linear chains, provided $|U|$ is large enough.

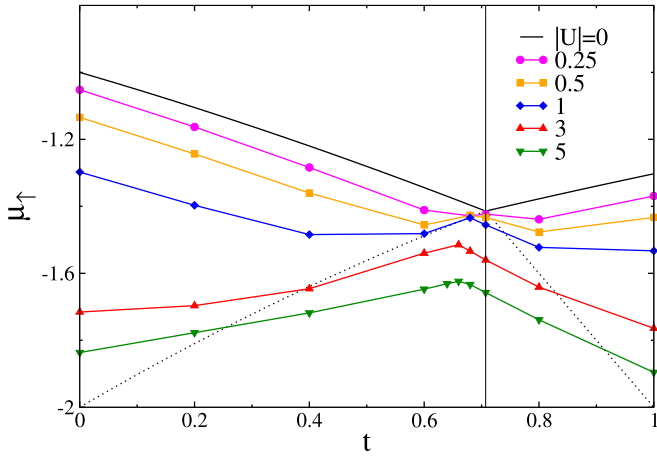


FIG. 12. Excess energy vs tunneling rate for different values of $U = 0, -0.25, -0.5, -1, -3, -5$ with $n_\uparrow = n_\downarrow = 1/3$. The dotted line represents the energy bottom $E_{\text{ref}}/2$ of the lower band. The vertical solid line indicates the flat-band point $t = 1/\sqrt{2}$. The connecting lines are a guide to the eye.

V. THREE-BODY BOUND STATES

In this section, we consider two spin-up fermions and one spin-down fermion, obeying the Hamiltonian (28), and we show that the fermion-pair anomalous attraction can induce the formation of a three-body bound state in vacuum (see [54–58] for earlier studies of trimers in 1D fermionic or bosonic lattice models). The binding energy E_b^{trimer} of the trimer is defined as

$$E_b^{\text{trimer}} = -E(2, 1) + E(1, 1) + E(1, 0), \quad (34)$$

under the assumption that the length L of the chain is infinite. We calculate the ground-state energy $E(2, 1)$ of the system numerically, based on the DMRG method, and we extract E_b^{trimer} from Eq. (34). The obtained results for $t = 1/\sqrt{2}$ are displayed in Fig. 13 as a function of the interaction strength, confirming the existence of trimers at the FB point. While

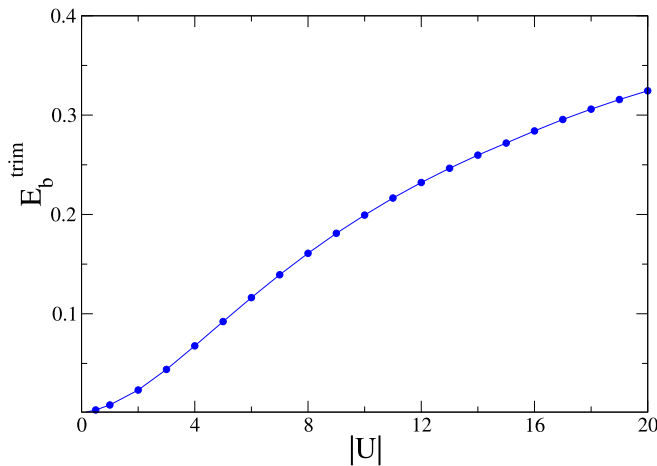


FIG. 13. Binding energy of a three-body bound state (trimer) at the flat-band point $t = 1/\sqrt{2}$ plotted as a function of the modulus of the interaction strength. The connecting line is a guide to the eye. The binding energy saturates to a constant $C \simeq 0.531$ for $|U| = \infty$.

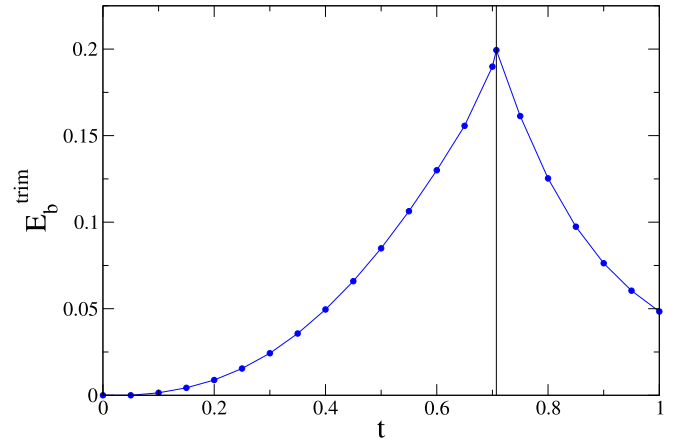


FIG. 14. Binding energy of the trimer as a function of the tunneling rate t for $U = -10$. The connecting line is a guide to the eye. The vertical line represents the flat-band point $t = 1/\sqrt{2}$.

in the strong-coupling regime the pair binding energy can become arbitrarily large, since $E_b \sim |U|$, this is not the case for trimers. Due to the Pauli exclusion principle, the pair and the extra fermion are separated by at least one lattice site, implying that the binding energy of the trimer must saturate to a constant value. Our DMRG calculations indicate that $E_b^{\text{trimer}}(U = -\infty) \approx 0.531$.

By continuity arguments, we expect that trimers exist for $t \neq 1/\sqrt{2}$ provided $|U|$ is large enough. In Fig. 14 we show the binding energy of the trimer as a function of the tunneling rate t for a fixed value of the interaction strength $U = -10$. We see that E_b^{trimer} is peaked at the FB point, in complete analogy with the two-body binding energy. Moreover, trimers break down near the integrable point, $t = 0$, in agreement with the Bethe ansatz solution.

Trimers in spin-1/2 fermionic systems arise from a subtle combination of Hubbard interactions and tunneling processes, similarly to trions in semiconductors, where the constituent particles are the exciton (electron-hole pair) and an extra charge (electron or hole). When two spin-up fermions are on neighboring sites, the spin-down fermion can decrease its kinetic energy by delocalizing between them, without changing the double occupancy. In the linear chain geometry, this effect cannot occur because the energy gain due to the delocalization of the spin-down fermion is exactly compensated by the energy cost to approach the two spin-up fermions. Trimers can nevertheless appear if the spin-up component is heavier than the spin-down counterpart, that is, if it possesses a larger effective mass [56,59–62] (see also [63] for an equivalent result for continuous 1D models). A strong attractive atom-dimer interaction has indeed been observed experimentally [64] in Fermi-Fermi mixtures of ultracold atoms with unequal masses, although in higher (three) dimensions. Our DMRG results establish that the constraint of unequal masses for the existence of trimers is no longer necessary in multiband systems.

We can better understand the formation of trimers starting from the strong-coupling regime $|U| \gg 1, t$. Since the pair is strongly bound, due to energy conservation it can never break

in vacuum. We therefore consider a class of three-body states,

$$e_r^{\sigma\sigma'\dagger} = \sum_i c_{i\uparrow}^{\sigma\dagger} c_{i\downarrow}^{\sigma'\dagger} c_{i+r\uparrow}^{\sigma'\dagger} | \rangle, \quad (35)$$

describing a pair sitting in the σ sublattice, with the extra spin-up fermion living in the sublattice σ' at a distance r from the dimer (the symbol $| \rangle$ refers to the vacuum state). Notice that, due to the Pauli exclusion principle, we have $e_0^{AA\dagger} = e_0^{BB\dagger} = 0$. We write the Hamiltonian (28) as a sum of two terms, $H = H_t + H_U$, where H_t describes tunneling processes while H_U accounts for the Hubbard interaction. We note that the states in Eq. (35) are all eigenstates of H_U with eigenvalue U . The variational ground-state energy of the trimer can then be obtained from degenerate perturbation theory as $E(2, 1) \approx U + \lambda_t$, where λ_t is the lowest eigenvalue of the following block matrix:

$$\mathcal{M} = \begin{pmatrix} e_i^{AA} H_t e_r^{AA\dagger} & e_i^{AA} H_t e_r^{AB\dagger} & e_i^{AA} H_t e_r^{BA\dagger} & e_i^{AA} H_t e_r^{BB\dagger} \\ e_i^{AB} H_t e_r^{AA\dagger} & e_i^{AB} H_t e_r^{AB\dagger} & e_i^{AB} H_t e_r^{BA\dagger} & e_i^{AB} H_t e_r^{BB\dagger} \\ e_i^{BA} H_t e_r^{AA\dagger} & e_i^{BA} H_t e_r^{AB\dagger} & e_i^{BA} H_t e_r^{BA\dagger} & e_i^{BA} H_t e_r^{BB\dagger} \\ e_i^{BB} H_t e_r^{AA\dagger} & e_i^{BB} H_t e_r^{AB\dagger} & e_i^{BB} H_t e_r^{BA\dagger} & e_i^{BB} H_t e_r^{BB\dagger} \end{pmatrix}. \quad (36)$$

To evaluate \mathcal{M} , we need to know how the tunneling Hamiltonian acts on a generic state (35). When H_t acts on the spin-up fermion forming the pair, it produces a state of zero double occupancy, which is orthogonal to the basis, so these processes can be neglected. The situation is different when H_t acts on the spin-down fermion, because the latter could land on a neighboring site that is already occupied by the second spin-up fermion. In this case, the pair and the extra fermion simply exchange their positions. Within the subspace of one double occupancy, we find

$$\begin{aligned} H_t e_r^{AA\dagger} &= e_r^{AB\dagger} + e_{r+1}^{AB\dagger}, \\ H_t e_r^{AB\dagger} &= e_{r-1}^{AA\dagger} + e_r^{AA\dagger} + t e_{r-1}^{AB\dagger} + t e_{r+1}^{AB\dagger} \\ &\quad - \delta_{r,1} e_{-1}^{BA\dagger} - \delta_{r,0} e_0^{BA\dagger}, \\ H_t e_r^{BA\dagger} &= -\delta_{r,0} e_0^{AB\dagger} - \delta_{r,-1} e_1^{AB\dagger} + e_r^{BB\dagger} + e_{r+1}^{BB\dagger}, \\ H_t e_r^{BB\dagger} &= e_{r-1}^{BA\dagger} + e_r^{BA\dagger} + t e_{r-1}^{BB\dagger} + t e_{r+1}^{BB\dagger} \\ &\quad - t \delta_{r,1} e_{-1}^{BB\dagger} - t \delta_{r,-1} e_1^{BB\dagger}. \end{aligned} \quad (37)$$

The terms on the right-hand side of Eqs. (37) with a negative sign originate from the exchange processes between the pair and the extra spin-up fermion, which can only occur if $r = 0$ or ± 1 . For instance, the first negative term in the third line of Eqs. (37) comes from $\sum_j c_{j+1\downarrow}^{B\dagger} c_{j\downarrow}^A e_r^{AB\dagger} = \sum_i c_{i\downarrow}^A c_{i+1\downarrow}^{B\dagger} c_{i+r\uparrow}^{\dagger} | \rangle = -\delta_{r,1} e_{-1}^{BA\dagger}$.

By using Eqs. (37), it is now straightforward to evaluate all the entries of \mathcal{M} . Notice that many blocks are actually null matrices; for instance, in the first row of Eq. (36) only one block (the second) is nonzero. We diagonalize the matrix (36) numerically after introducing a cutoff integer N for the relative distance between the pair and the extra spin-up fermion, thus limiting the size of each block according to $|i|, |r| \leq N$. For a given N , \mathcal{M} is a square matrix of dimension $8N + 2$. We extract its lowest eigenvalue by choosing N large enough to ensure full convergence and extract the binding energy from Eq. (34). The obtained results as a function of

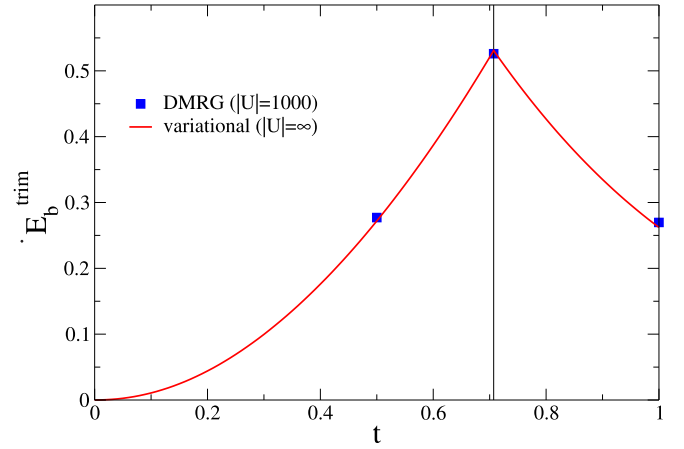


FIG. 15. Binding energy of the trimer as a function of the tunneling rate t . The solid line is the prediction of the variational approach for infinite attraction, obtained by diagonalizing the Hamiltonian over the class of three-body states in Eq. (35). The square symbols are DMRG results for three different values of $t = 1/2, 1/\sqrt{2}, 1$ and $U = -1000$. The vertical line represents the flat-band point $t = 1/\sqrt{2}$.

the tunneling rate are shown in Fig. 15 by the solid line. We see that our variational approach for $U = -\infty$ reproduces all the expected features, notably the absence of trimers for $t = 0$ and the peak in the three-body binding energy at the FB point. For $t = 1/\sqrt{2}$ it gives $E_b^{\text{trim}} \approx 0.53087$, which is in very good agreement with the DMRG data for $U = -1000$ (square symbols). Moving away from the FB point, the variational approach slightly underestimates the binding energy of the trimer. A fit to the numerical results for small t reveals that the binding energy of the trimer, calculated within the variational approach, vanishes as t^2 approaches the integrable point, $t = 0$. This result implies that, for infinite attraction, trimers exist for any nonzero value of t .

Our numerics shows that the convergence of the binding energy as a function of the cutoff N is particularly fast approaching the FB point. Indeed using $N = 1$ yields $E_b^{\text{trim}} \approx 0.51317$, corresponding to a relative error of only 3%. In this case, the matrix in Eq. (36) reduces to the 10×10 matrix

$$\mathcal{M} = \begin{pmatrix} 0 & 0 & 1 & 1 & 0 & 0 & 0 & 0 & 0 & 0 \\ 0 & 0 & 0 & 0 & 1 & 0 & 0 & 0 & 0 & 0 \\ 1 & 0 & 0 & t & 0 & 0 & 0 & 0 & 0 & 0 \\ 0 & 1 & 0 & t & 0 & 0 & -1 & 0 & 0 & 0 \\ 0 & 0 & 0 & 0 & -1 & 0 & 0 & 0 & 0 & 0 \\ 0 & 0 & 0 & -1 & 0 & 0 & 0 & 0 & 0 & 1 \\ 0 & 0 & 0 & 0 & 0 & 0 & 0 & 0 & 0 & 1 \\ 0 & 0 & 0 & 0 & 0 & 1 & 0 & 0 & 0 & -t \\ 0 & 0 & 0 & 0 & 0 & 0 & 1 & 1 & -t & 0 \end{pmatrix}. \quad (38)$$

By moving away from the FB point, the value of N needed to ensure convergence becomes larger and larger, signaling that the mean distance between the pair and the extra fermion increases and the binding energy is reduced.

VI. CONCLUSION AND OUTLOOK

In this work, we have investigated the Fermi-Hubbard model with attractive interactions on a 1D sawtooth lattice. From the solution of the two-body problem, we have extracted the binding energy and the effective mass of the pair, both analytically and numerically. We have shown that, in a broad region of t values around the FB point, both quantities are highly sensitive to weak interactions. In particular, the binding energy possesses a pronounced maximum in correspondence with the FB point, $t = 1/\sqrt{2}$, which persists for any $U < 0$. From the inverse effective mass of the pair at the FB point, we have estimated the superfluid weight D_s of the many-body system, showing that it is in good agreement with the DMRG calculations of [30].

Our numerical results for fully paired many-body systems reveal that the proximity to a flat band significantly modifies the nature of the BCS-BEC crossover. While the chemical potential remains always pinned near its two-body value, the pairing gap is strongly depleted at finite density and takes its maximum value not at the FB point, but at a shifted position $t^* < 1/\sqrt{2}$, which depends on the value of the density. We show that the anomalous pairing in the sawtooth lattice comes from the fact that the energy change upon adding an extra spin-up fermion to the system falls below the bottom of the single-particle spectrum, $\mu_\uparrow < E_{\text{ref}}/2$, causing the appearance of an effective attraction between the pairs in the medium and the excess fermion. Importantly, we have unveiled that a spin-down fermion and two spin-up fermions in the sawtooth lattice can form a three-body bound state, whose binding energy is also peaked at the FB point and vanishes at the integrable point, $t = 0$. Our results establish that trimers exist in flat-band lattices and they are detrimental to superconductivity.

It would be interesting to study by exact numerics the behavior of the superfluid weight D_s in the sawtooth lattice for a generic tunneling rate and its relation with the pair inverse effective mass. Our results show that for finite $|U|$, the minimum of $1/m_p^*$ drifts towards smaller values of t . Another intriguing direction is to understand whether multiband BCS theory can correctly predict the anomalous behavior of the pairing gap observed in our numerics, especially at low density.

The results discussed in this work can be investigated experimentally with cold atoms in optical lattices. In particular, a viable scheme to implement the sawtooth lattice has been recently proposed [41,65]. The interaction strength can be controlled either directly, via a Feshbach resonance, or indirectly, by varying the tunneling rates t, t' and consequently the ratios t/U and t'/U . While we have mainly focused on the sawtooth lattice, we expect that our results will apply also to other FB systems.

Note added: The existence of trimers in the 1D sawtooth lattice at the FB point has been confirmed in a very recent paper [66] by Iskin, reporting a very good agreement with our DMRG results displayed in Fig. 13. In that work, the three-body problem is solved numerically by mapping it into an effective integral equation [54,56], and the presence of trimers for other values of the tunneling rates has also been discussed.

ACKNOWLEDGMENTS

We thank S. Pilati and F. Chevy for useful comments on the manuscript. G.O. acknowledges financial support from ANR (Grant SpiFBox) and from DIM Sirteq (Grant EML 19002465 1DFG). M.S. acknowledges funding from a MULTIPLY postdoctoral fellowship under the Marie Skłodowska-Curie COFUND Action (Grant Agreement No. 713694).

-
- [1] D. Leykam, A. Andreanov, and S. Flach, Artificial flat band systems: from lattice models to experiments, *Adv. Phys.: X* **3**, 1473052 (2018).
 - [2] V. A. Khodel and V. R. Shaginyan, Superfluidity in system with fermion condensate, *JETP Lett.* **51**, 553 (1990).
 - [3] N. B. Kopnin, T. T. Heikkilä, and G. E. Volovik, High-temperature surface superconductivity in topological flat-band systems, *Phys. Rev. B* **83**, 220503(R) (2011).
 - [4] T. T. Heikkilä, N. B. Kopnin, and G. E. Volovik, Flat bands in topological media, *JETP Lett.* **94**, 233 (2011).
 - [5] H. Aoki, Theoretical possibilities for flat band superconductivity, *J. Supercond. Novel Magn.* **33**, 2341 (2020).
 - [6] E. Tang, J.-W. Mei, and X.-G. Wen, High-Temperature Fractional Quantum Hall States, *Phys. Rev. Lett.* **106**, 236802 (2011).
 - [7] G.-B. Jo, J. Guzman, C. K. Thomas, P. Hosur, A. Vishwanath, and D. M. Stamper-Kurn, Ultracold Atoms in a Tunable Optical Kagome Lattice, *Phys. Rev. Lett.* **108**, 045305 (2012).
 - [8] S. Taie, H. Ozawa, T. Ichinose, T. Nishio, S. Nakajima, and Y. Takahashi, Coherent driving and freezing of bosonic matter wave in an optical lieb lattice, *Sci. Adv.* **1**, e1500854 (2015).
 - [9] T.-H. Leung, M. N. Schwarz, S.-W. Chang, C. D. Brown, G. Unnikrishnan, and D. Stamper-Kurn, Interaction-Enhanced Group Velocity of Bosons in the Flat Band of an Optical Kagome Lattice, *Phys. Rev. Lett.* **125**, 133001 (2020).
 - [10] H. Gersen, T. J. Karle, R. J. P. Engelen, W. Bogaerts, J. P. Korterik, N. F. van Hulst, T. F. Krauss, and L. Kuipers, Real-Space Observation of Ultraslow Light in Photonic Crystal Waveguides, *Phys. Rev. Lett.* **94**, 073903 (2005).
 - [11] S. Mukherjee, A. Spracklen, D. Choudhury, N. Goldman, P. Öhberg, E. Andersson, and R. R. Thomson, Observation of a Localized Flat-Band State in a Photonic Lieb Lattice, *Phys. Rev. Lett.* **114**, 245504 (2015).
 - [12] T. Jacqmin, I. Carusotto, I. Sagnes, M. Abbarchi, D. D. Solnyshkov, G. Malpuech, E. Galopin, A. Lemaître, J. Bloch, and A. Amo, Direct Observation of Dirac Cones and a Flatband in a Honeycomb Lattice for Polaritons, *Phys. Rev. Lett.* **112**, 116402 (2014).
 - [13] R. Drost, T. Ojanen, A. Harju, and P. Liljeroth, Topological states in engineered atomic lattices, *Nat. Phys.* **13**, 668 (2017).
 - [14] M. R. Slot, T. S. Gardenier, P. H. Jacobse, G. C. P. van Miert, S. N. Kempkes, S. J. M. Zevenhuizen, C. M. Smith, D. Vanmaekelbergh, and I. Swart, Experimental realization and characterization of an electronic lieb lattice, *Nat. Phys.* **13**, 672 (2017).

- [15] M. N. Huda, S. Kezilebieke, and P. Liljeroth, Designer flat bands in quasi-one-dimensional atomic lattices, *Phys. Rev. Research* **2**, 043426 (2020).
- [16] Y. Cao, V. Fatemi, S. Fang, K. Watanabe, T. Taniguchi, E. Kaxiras, and P. Jarillo-Herrero, Unconventional superconductivity in magic-angle graphene superlattices, *Nature (London)* **556**, 43 (2018).
- [17] G. Salerno, G. Palumbo, N. Goldman, and M. Di Liberto, Interaction-induced lattices for bound states: Designing flat bands, quantized pumps, and higher-order topological insulators for doublons, *Phys. Rev. Research* **2**, 013348 (2020).
- [18] Y. Kuno, T. Mizoguchi, and Y. Hatsugai, Interaction-induced doublons and embedded topological subspace in a complete flat-band system, *Phys. Rev. A* **102**, 063325 (2020).
- [19] S. Flannigan and A. J. Daley, Enhanced repulsively bound atom pairs in topological optical lattice ladders, *Quantum Sci. Technol.* **5**, 045017 (2020).
- [20] G. Pelegrí, A. M. Marques, V. Ahufinger, J. Mompart, and R. G. Dias, Interaction-induced topological properties of two bosons in flat-band systems, *Phys. Rev. Research* **2**, 033267 (2020).
- [21] P. Törmä, L. Liang, and S. Peotta, Quantum metric and effective mass of a two-body bound state in a flat band, *Phys. Rev. B* **98**, 220511(R) (2018).
- [22] M. Iskin, Two-body problem in a multiband lattice and the role of quantum geometry, *Phys. Rev. A* **103**, 053311 (2021).
- [23] M. Iskin, Effective-mass tensor of the two-body bound states and the quantum-metric tensor of the underlying Bloch states in multiband lattices, *Phys. Rev. A* **105**, 023312 (2022).
- [24] S. Peotta and P. Törmä, Superfluidity in topologically nontrivial flat bands, *Nat. Commun.* **6**, 8944 (2015).
- [25] A. Julku, S. Peotta, T. I. Vanhala, D.-H. Kim, and P. Törmä, Geometric Origin of Superfluidity in the Lieb-Lattice Flat Band, *Phys. Rev. Lett.* **117**, 045303 (2016).
- [26] R. Mondaini, G. G. Batrouni, and B. Grémaud, Pairing and superconductivity in the flat band: Creutz lattice, *Phys. Rev. B* **98**, 155142 (2018).
- [27] M. Iskin, Superfluid stiffness for the attractive Hubbard model on a honeycomb optical lattice, *Phys. Rev. A* **99**, 023608 (2019).
- [28] L. Balents, C. R. Dean, D. K. Efetov, and A. F. Young, Superconductivity and strong correlations in moiré flat bands, *Nat. Phys.* **16**, 725 (2020).
- [29] N. Verma, T. Hazra, and M. Randeria, Optical spectral weight, phase stiffness, and T_c bounds for trivial and topological flat band superconductors, *Proc. Natl. Acad. Sci. (USA)* **118**, e2106744118 (2021).
- [30] S. M. Chan, B. Grémaud, and G. G. Batrouni, Pairing and superconductivity in quasi-one-dimensional flat-band systems: Creutz and sawtooth lattices, *Phys. Rev. B* **105**, 024502 (2022).
- [31] V. A. J. Pyykkönen, S. Peotta, P. Fabritius, J. Mohan, T. Esslinger, and P. Törmä, Flat-band transport and Josephson effect through a finite-size sawtooth lattice, *Phys. Rev. B* **103**, 144519 (2021).
- [32] J. S. Hofmann, E. Berg, and D. Chowdhury, Superconductivity, pseudogap, and phase separation in topological flat bands, *Phys. Rev. B* **102**, 201112(R) (2020).
- [33] V. Peri, Z.-D. Song, B. A. Bernevig, and S. D. Huber, Fragile Topology and Flat-Band Superconductivity in the Strong-Coupling Regime, *Phys. Rev. Lett.* **126**, 027002 (2021).
- [34] R. Micnas, J. Ranninger, and S. Robaszkiewicz, Superconductivity in narrow-band systems with local nonretarded attractive interactions, *Rev. Mod. Phys.* **62**, 113 (1990).
- [35] I. Bloch, J. Dalibard, and W. Zwerger, Many-body physics with ultracold gases, *Rev. Mod. Phys.* **80**, 885 (2008).
- [36] M. Iskin, Two-band superfluidity and intrinsic Josephson effect in alkaline-earth-metal Fermi gases across an orbital Feshbach resonance, *Phys. Rev. A* **94**, 011604(R) (2016).
- [37] L. He, J. Wang, S.-G. Peng, X.-J. Liu, and H. Hu, Strongly correlated Fermi superfluid near an orbital Feshbach resonance: Stability, equation of state, and Leggett mode, *Phys. Rev. A* **94**, 043624 (2016).
- [38] J. Xu, R. Zhang, Y. Cheng, P. Zhang, R. Qi, and H. Zhai, Reaching a Fermi-superfluid state near an orbital Feshbach resonance, *Phys. Rev. A* **94**, 033609 (2016).
- [39] H. Tajima, Y. Yerin, A. Perali, and P. Pieri, Enhanced critical temperature, pairing fluctuation effects, and BCS-BEC crossover in a two-band Fermi gas, *Phys. Rev. B* **99**, 180503(R) (2019).
- [40] H. Tajima, A. Perali, and P. Pieri, BCS-BEC crossover and pairing fluctuations in a two band superfluid/superconductor: A t matrix approach, *Condens. Matter* **5**, 10 (2020).
- [41] S. D. Huber and E. Altman, Bose condensation in flat bands, *Phys. Rev. B* **82**, 184502 (2010).
- [42] Y.-Z. You, Z. Chen, X.-Q. Sun, and H. Zhai, Superfluidity of Bosons in Kagome Lattices with Frustration, *Phys. Rev. Lett.* **109**, 265302 (2012).
- [43] L. G. Phillips, G. De Chiara, P. Öhberg, and M. Valiente, Low-energy behavior of strongly interacting bosons on a flat-band lattice above the critical filling factor, *Phys. Rev. B* **91**, 054103 (2015).
- [44] F. Baboux, L. Ge, T. Jacqmin, M. Biondi, E. Galopin, A. Lemaître, L. Le Gratiet, I. Sagnes, S. Schmidt, H. E. Türeci, A. Amo, and J. Bloch, Bosonic Condensation and Disorder-Induced Localization in a Flat Band, *Phys. Rev. Lett.* **116**, 066402 (2016).
- [45] H. Ozawa, S. Taie, T. Ichinose, and Y. Takahashi, Interaction-Driven Shift and Distortion of a Flat Band in an Optical Lieb Lattice, *Phys. Rev. Lett.* **118**, 175301 (2017).
- [46] M. Wouters and G. Orso, Two-body problem in periodic potentials, *Phys. Rev. A* **73**, 012707 (2006).
- [47] G. Dufour and G. Orso, Anderson Localization of Pairs in Bichromatic Optical Lattices, *Phys. Rev. Lett.* **109**, 155306 (2012).
- [48] M. Valiente and N. T. Zinner, Quantum collision theory in flat bands, *J. Phys. B* **50**, 064004 (2017).
- [49] G. Orso and G. V. Shlyapnikov, Superfluid Fermi Gas in a 1D Optical Lattice, *Phys. Rev. Lett.* **95**, 260402 (2005).
- [50] M. Tovmasyan, S. Peotta, P. Törmä, and S. D. Huber, Effective theory and emergent SU(2) symmetry in the flat bands of attractive Hubbard models, *Phys. Rev. B* **94**, 245149 (2016).
- [51] F. Marsiglio, Evaluation of the BCS approximation for the attractive Hubbard model in one dimension, *Phys. Rev. B* **55**, 575 (1997).
- [52] F. Heidrich-Meisner, G. Orso, and A. E. Feiguin, Phase separation of trapped spin-imbalanced Fermi gases in one-dimensional optical lattices, *Phys. Rev. A* **81**, 053602 (2010).
- [53] F. Woynarovich and K. Penc, Novel magnetic properties of the Hubbard chain with an attractive interaction, *Z. Phys. B* **85**, 269 (1991).

- [54] D. C. Mattis, The few-body problem on a lattice, *Rev. Mod. Phys.* **58**, 361 (1986).
- [55] E. Burovski, G. Orso, and T. Jolicoeur, Multiparticle Composites in Density-Imbalanced Quantum Fluids, *Phys. Rev. Lett.* **103**, 215301 (2009).
- [56] G. Orso, E. Burovski, and T. Jolicoeur, Luttinger Liquid of Trimers in Fermi Gases with Unequal Masses, *Phys. Rev. Lett.* **104**, 065301 (2010).
- [57] M. Valiente, D. Petrosyan, and A. Saenz, Three-body bound states in a lattice, *Phys. Rev. A* **81**, 011601(R) (2010).
- [58] M. Dalmonte, P. Zoller, and G. Pupillo, Trimer Liquids and Crystals of Polar Molecules in Coupled Wires, *Phys. Rev. Lett.* **107**, 163202 (2011).
- [59] G. Orso, E. Burovski, and T. Jolicoeur, Fermionic trimers in spin-dependent optical lattices, *CRAS (Paris) Phys.* **12**, 39 (2011).
- [60] G. Roux, E. Burovski, and T. Jolicoeur, Multimer formation in one-dimensional two-component gases and trimer phase in the asymmetric attractive Hubbard model, *Phys. Rev. A* **83**, 053618 (2011).
- [61] M. Dalmonte, K. Dieckmann, T. Roscilde, C. Hartl, A. E. Feiguin, U. Schollwöck, and F. Heidrich-Meisner, Dimer, trimer, and Fulde-Ferrell-Larkin-Ovchinnikov liquids in mass- and spin-imbalanced trapped binary mixtures in one dimension, *Phys. Rev. A* **85**, 063608 (2012).
- [62] A. Dhar, P. Törmä, and J. J. Kinnunen, Fast trimers in a one-dimensional extended Fermi-Hubbard model, *Phys. Rev. A* **97**, 043624 (2018).
- [63] O. I. Kartavtsev, A. V. Malykh, and S. A. Sofianos, Bound states and scattering lengths of three two-component particles with zero-range interactions under one-dimensional confinement, *J. Exp. Theor. Phys.* **108**, 365 (2009).
- [64] M. Jag, M. Zaccanti, M. Cetina, R. S. Lous, F. Schreck, R. Grimm, D. S. Petrov, and J. Levinsen, Observation of a Strong Atom-Dimer Attraction in a Mass-Imbalanced Fermi-Fermi Mixture, *Phys. Rev. Lett.* **112**, 075302 (2014).
- [65] T. Zhang and G.-B. Jo, One-dimensional sawtooth and zigzag lattices for ultracold atoms, *Sci. Rep.* **5**, 16044 (2015).
- [66] M. Iskin, Three-body problem in a multiband Hubbard model, *Phys. Rev. A* **105**, 063310 (2022).